Structural Engineering and Mechanics, *Vol. 99, No. 2 (2026) 287-311*
https://doi.org/10.12989/sem.2026.99.2.287

Techno-Press

Practical multi-objective optimal design of 3D reinforced concrete moment frames using NSGA-II

Jaemin So[1], Seungjae Lee[1], Koichi Kusunoki[2], Donwoo Lee*[1]

[1]Future Convergence Engineering, Department of Architectural Engineering, KOREATECH, Cheonan, 31253, Chungcheongnam-do, Republic of Korea
[2]Earthquake Research Institute, The University of Tokyo, Tokyo, 113-0032, Japan

(Received March 20, 2026, Revised June 23, 2026, Accepted June 26, 2026)

Abstract. This study presents a practical multi-objective optimization framework for 3D reinforced concrete (RC) moment-resisting frames using NSGA-II. Its main novelty is a decoupled genetic encoding of column rotation angles (0°/90°), combined with a section database that embeds ACI 318-19 reinforcement detailing—crossties, skin reinforcement, and seismic hooks—directly as discrete design variables. Two objectives are minimized: a normalized sum of total construction cost and embodied CO_2, and the maximum inter-story drift ratio. On 4-, 6-, and 8-story irregular benchmark frames, the decoupled approach (Scenario A) attains a 4.5% higher Hypervolume and up to 22% lower cost at equal drift than the conventional coupled approach (Scenario B), and ten independent runs confirm convergence robustness. Construction cost and embodied CO_2 are found to be almost perfectly correlated ($R^2 \geq 0.99$), so the effective trade-off is between the combined cost–carbon objective and drift; the study also quantifies how the design freedom of this trade-off contracts as building height increases.

Keywords: column rotation; genetic encoding strategy; multi-objective optimization; NSGA-II; Pareto optimization; reinforced concrete; section database; structural design

1. Introduction

Reinforced concrete (RC) moment-resisting frames are widely employed as a core structural system in modern buildings owing to their superior structural stiffness and economic efficiency. However, the growing trend toward taller and more irregular buildings driven by urbanization has increasingly complicated the process of finding an optimal balance between the conflicting objectives of cost reduction and structural safety during the design stage [1-3]. Conventional design approaches rely on engineers' empirical judgment to perform conservative designs followed by iterative refinements; however, this process has clear limitations in guaranteeing a global optimum within the vast three-dimensional design space encompassing numerous design variables.

Recent efforts to overcome these limitations have been sustained through the introduction of metaheuristic optimization techniques, such as Genetic Algorithms and Particle Swarm Optimization (PSO), into the structural engineering domain [4-12]. In particular, NSGA-II (Non-

*Corresponding author, Ph.D., E-mail: lov1004ely@koreatech.ac.kr

http://www.techno-press.org/sem/5 ISSN: 1225-4568 (Print), 1598-6217 (Online)

dominated Sorting Genetic Algorithm II) is recognized as a powerful algorithm capable of efficiently deriving Pareto optimal solutions in multi-objective optimization problems [13-16]. Beyond drift- and cost-based objectives, recent multi-objective studies have also incorporated life-cycle cost and performance, as well as advanced metaheuristics, into RC structural design. Nevertheless, existing RC structural optimization studies possess several significant limitations from the perspective of practical application.

A substantial portion of existing studies has been confined to two-dimensional (2D) frame models, limiting the scope of design variable optimization accordingly. Real buildings behave in three-dimensional space, where torsion induced by lateral forces and stiffness variations due to column orientation critically affect the overall structural system efficiency. Moreover, many studies have simplified cross-sections to square shapes or arbitrarily fixed the strong-axis direction of columns, thereby fundamentally precluding opportunities for structural optimization through aspect ratio adjustment and column rotation [17-28]. Finally, overly simplified cost estimation models have failed to account for crossties, skin reinforcement, and seismic detail hooks required by practical design codes, resulting in significant discrepancies between optimization results and actual construction quantities [29-31].

To address these research gaps, this study proposes a multi-objective optimization framework that can be immediately applied to practical structural design. The distinctive features of this study lie in the utilization of a detailed section database—incorporating bidirectional and unidirectional reinforcement patterns for column sections, as well as automatic placement logic for skin reinforcement and crossties—as design variables. Furthermore, to efficiently address the directional stiffness demand differences arising from practical design conditions, such as floor-wise live load variations due to different occupancy types and unbalanced checkerboard loading patterns, a binary rotation variable determining the strong-axis direction of columns was introduced. This variable efficiently addresses the directional stiffness demand differences that arise from practical design conditions, such as floor-wise live load variations due to different occupancy types and unbalanced checkerboard loading patterns. This enables the algorithm to actively explore optimal member orientations according to the local loading conditions of each floor. In addition, a quantity estimation engine strictly complying with ACI 318-19 seismic detailing was developed to ensure the reliability of economic evaluations [32-36].

2. Problem formulation

2.1 Design variables and chromosome structure

In this study, instead of continuous variables, database indices representing a set of discrete, practically constructible sections are adopted as design variables. In particular, to efficiently control the vast search space of the three-dimensional frame and to ensure constructability, a grouping strategy that accounts for the floor-wise location and plan-wise geometric arrangement of members is introduced. The overall design variable vector X is defined as in Eq. (1).

$$X = \left[C_{id_n}, R_{dir_n}, B_{id_m}\right]^T \tag{1}$$

where C_{id} denotes the index of the column section database, R_{dir} is a binary variable determining the rotation of the column (0: 0°, 1: 90°), and B_{id} represents the index of the beam section database. Because the rotation variable R_{dir} is encoded as a gene separate from the section index

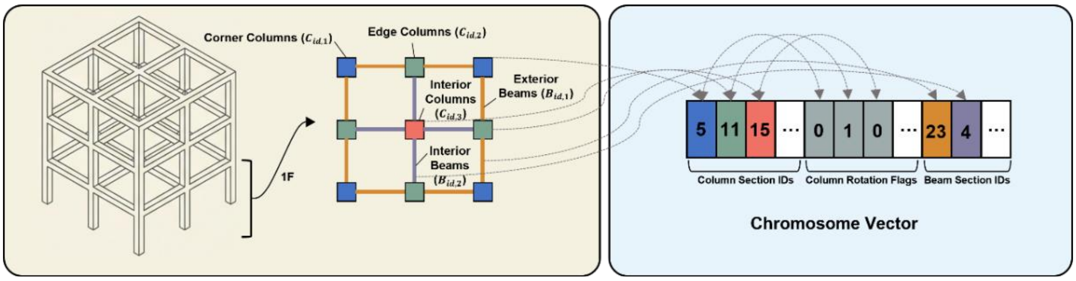

Figure 1. Mapping mechanism from 3D frame member grouping to the genetic chromosome structure

C_{id}—rather than being embedded within a section database pre-expanded to include both orientations—this scheme is referred to as a decoupled rotation gene. This separation allows the algorithm to search the section type and its orientation independently, which is the central encoding innovation of this study (its effect is quantified in Section 5.2). As illustrated in Fig. 1, each member group is hierarchically classified according to the building height (story) and the load-sharing characteristics in the horizontal plane, as follows:

Column Groups: The columns at each story are classified into three types based on their plan location: Corner columns, Edge columns, and Interior columns. This classification is intended to precisely reflect the physical loading conditions—where the proportions of biaxial bending and axial force differ depending on the member location—within the optimization process.

Beam Groups: Beams are categorized into two types: Exterior beams, which are located along the plan perimeter and support slab loads in one direction, and Interior beams, which carry loads from both directions.

Through this strategy, the framework actively responds to the local load imbalance at each story while maintaining the total number of design variables at a level suitable for optimization, thereby enhancing the search efficiency of the algorithm. This position-wise grouping is grounded in mechanics: corner, edge, and interior columns sustain markedly different combinations of axial force and biaxial bending, and exterior versus interior beams differ in tributary width and one-versus two-way load paths, so grouping by physical role lets the optimizer assign suitable sections to each role—consistent with established automated member-grouping practice [30]. A coarser grouping (e.g., a single group per story) would merge mechanically distinct members and forfeit this distinction, whereas per-member variables would inflate the search space and degrade efficiency; the adopted scheme balances these competing demands. Fig. 1 illustrates how this physically motivated grouping strategy is mapped onto the chromosome structure of the genetic algorithm. The detailed composition range and generation logic of the section database assigned to each group are described in Section 4.1.

2.2 Objective functions

The first objective function (f_1) is a metric for the integrated evaluation of economic and environmental performance. In this study, recognizing that both total construction cost and carbon emissions are proportional to the quantity of materials used, the two indicators are combined and minimized without separate weighting factors. It should be emphasized that cost and CO_2 are not treated as two competing objectives: because both $Cost(X)$ (Eq. (3)) and $CO_2(X)$ (X) (Eq. (4)) are linear combinations of the identical set of member quantities (concrete volume, reinforcement

Table 1. Material properties, unit costs, and CO_2 emission factors

Material	Unit cost (C)	CO_2 factor (E)	Unit (C/E)
Concrete	80,000	0.15	KRW/m^3 kgCO$_2$e/kg
Steel Reinforcement	1,000,000	1.99	KRW/ton kgCO$_2$e/kg
Formwork	25,000	10.0	KRW/m^2 kgCO$_2$e/m^2

weight, and formwork area) using fixed unit coefficients (Table 1), the two are inherently strongly correlated by construction, and minimizing one necessarily reduces the other. They are therefore aggregated into a single economic–environmental objective, and the present problem is a genuinely two-objective optimization—combined economic–environmental impact (f_1) versus structural drift performance (f_2). The validity of this equal-weight summation is quantified in Section 5.1, where the magnitude of this structurally expected correlation is reported. However, because the inherent construction cost (KRW) and carbon emissions (kgCO$_2$e) defined for each section in the database differ in their numerical units and variational scales, each indicator is normalized by its minimum and maximum values within the design space prior to summation, so that both contribute equally. The first objective function f_1 is defined as in Eq. (2).

$$min f_1(X) = \frac{Cost(X) - C_{min}}{C_{max} - C_{min}} + \frac{CO_2(X) - E_{min}}{E_{max} - E_{min}} \tag{2}$$

where C_{min}, C_{max}, E_{min}, and E_{max} denote the minimum and maximum values of construction cost and carbon dioxide emissions, respectively, within the entire design space. The total construction cost $Cost(X)$ and total carbon emissions $CO_2(X)$ for the entire set of N members are computed as the summation of individual member quantities, as given in Eqs. (3) and (4).

$$Cost(X) = \sum_{k=1}^{N} \left(C_{conc} V_{c,k} + C_{steel} W_{s,k} + C_{form} A_{f,k} \right) \tag{3}$$

$$CO_2(X) = \sum_{k=1}^{N} \left(E_{conc} \left(\gamma_c V_{c,k} \right) + E_{steel} \left(W_{s,k} \cdot 10^3 \right) + E_{form} A_{f,k} \right) \tag{4}$$

In these expressions, $V_{c,k}$ is the net concrete volume (m^3) of the k-th member, $W_{s,k}$ is the reinforcement weight (kg), and $A_{f,k}$ is the formwork area (m^2). The reported construction cost refers to the cost of the structural frame members (columns and beams) only, and excludes non-structural and finishing costs. C and E represent the unit cost and carbon emission factor of the corresponding material, respectively, and the detailed parameters used for the calculation are summarized in Table 1.

The second objective function (f_2) is a metric for evaluating the safety and serviceability of the structure; it minimizes the maximum inter-story drift ratio across all stories to ensure adequate resistance to lateral forces. In this study, to achieve numerical scale balance with the first objective function and thereby enhance the search efficiency of the algorithm, the maximum inter-story drift ratio is normalized by the allowable limit θ_{allow} and defined as in Eq. (5).

$$min f_2(X) = \frac{max\left(\frac{\Delta_{i,k}}{H_k}\right)}{\theta_{allow}} \tag{5}$$

where $\Delta_{i,k}$ denotes the inter-story drift in the i-direction at the k-th story, and H_k is the

Table 2. Summary of structural design constraints expressed as $g_i(X) \leq 0$

Category	Constraint	Mathematical Expression (g_i)	Criteria	Reference
Strength	Member DCR	$g_1(X) = DCR - 1.0 \leq 0$	Max. DCR 1.0	ACI 318-19
Serviceability	Story Drift Ratio	$g_2(X) = \Delta/H - 0.020 \leq 0$	Max 2.0%	ASCE 7-16
Serviceability	Beam Deflection	$g_3(X) = (\delta_{LT} + \delta_{L,imm}) - L/240 \leq 0$	Long-term + LL	ACI 318-19
Serviceability	Wind Displacement	$g_4(X) = \Delta_{wind}/(H/400) - 1.0 \leq 0$	Max H/400	ASCE 7-16
Hierarchy	SCWB Ratio	$g_5(X) = \frac{1.2\sum M_{nb}}{\sum M_{nc}} - 1.0 \leq 0$	Strong Column	ACI 318-19

corresponding story height. Since the analysis in this study is performed under the assumption of rigid diaphragm behavior of the floor slabs, safety is evaluated using story-level displacement indices rather than the individual lateral displacements of each node. The allowable inter-story drift ratio θ_{allow} is set to 0.020 in accordance with ASCE 7-16 [37]. An f_2 value reaching 1.0 indicates that the maximum displacement permitted by the design code has been attained. The specific loading conditions and modeling parameters applied to the example structures are described in Appendix A.

2.3 Constraints

Strength, serviceability, and hierarchical structural constraints are imposed to ensure the practical validity of the design solution. In this study, the strong-column weak-beam (SCWB) design principle and the roof displacement constraint under wind loading are included to enhance the practical completeness of the framework. The detailed criteria for the major constraints considered and their mathematical formulations ($g_i(X) \leq 0$) for integration into the optimization algorithm are summarized in Table 2. Here, the strength constraint is expressed through the member demand-capacity ratio (DCR), defined as the ratio of the required strength to the design strength ($DCR = U/\phi R_n$). All constraints are considered satisfied when the corresponding expression evaluates to zero or less; violations are accumulated in proportion to the degree of violation into the total constraint violation measure ($\Phi(X)$). This value serves as a key indicator for determining individual selection and evolutionary direction under the constrained dominance principle described in Section 3.1.

The individual constraint violation is computed as $v_i(X) = max(0, g_i(X))$, and the total constraint violation ($\Phi(X)$), used to evaluate the feasibility of individuals within the algorithm, is calculated by normalizing the scale of each constraint as given in Eq. (6).

$$\Phi(X) = \sum_{i=1}^{m} \frac{v_i(X)}{S_i} \tag{6}$$

where m is the total number of constraints and S_i is the scaling factor for normalizing the violation of each constraint. For individuals satisfying all constraints, $\Phi(X) = 0$. The scaling factors adopted in this study are $S_1 = 1.0$ (member DCR), $S_2 = 0.020$ (story drift ratio), $S_3 = L/240$ (beam deflection), $S_4 = 1.0$ (wind displacement), and $S_5 = 0.2$ (SCWB ratio). These values normalize each violation term—whose physical magnitudes differ by several orders—so that all terms contribute comparably to $\Phi(X)$; here S_1 and S_4 equal 1.0 because g_1 and g_4 are already dimensionless ratios, while $S_5 = 0.2$ is set so that an SCWB ratio exceeding the limit by 0.2 contributes on par with the other strength and serviceability terms.

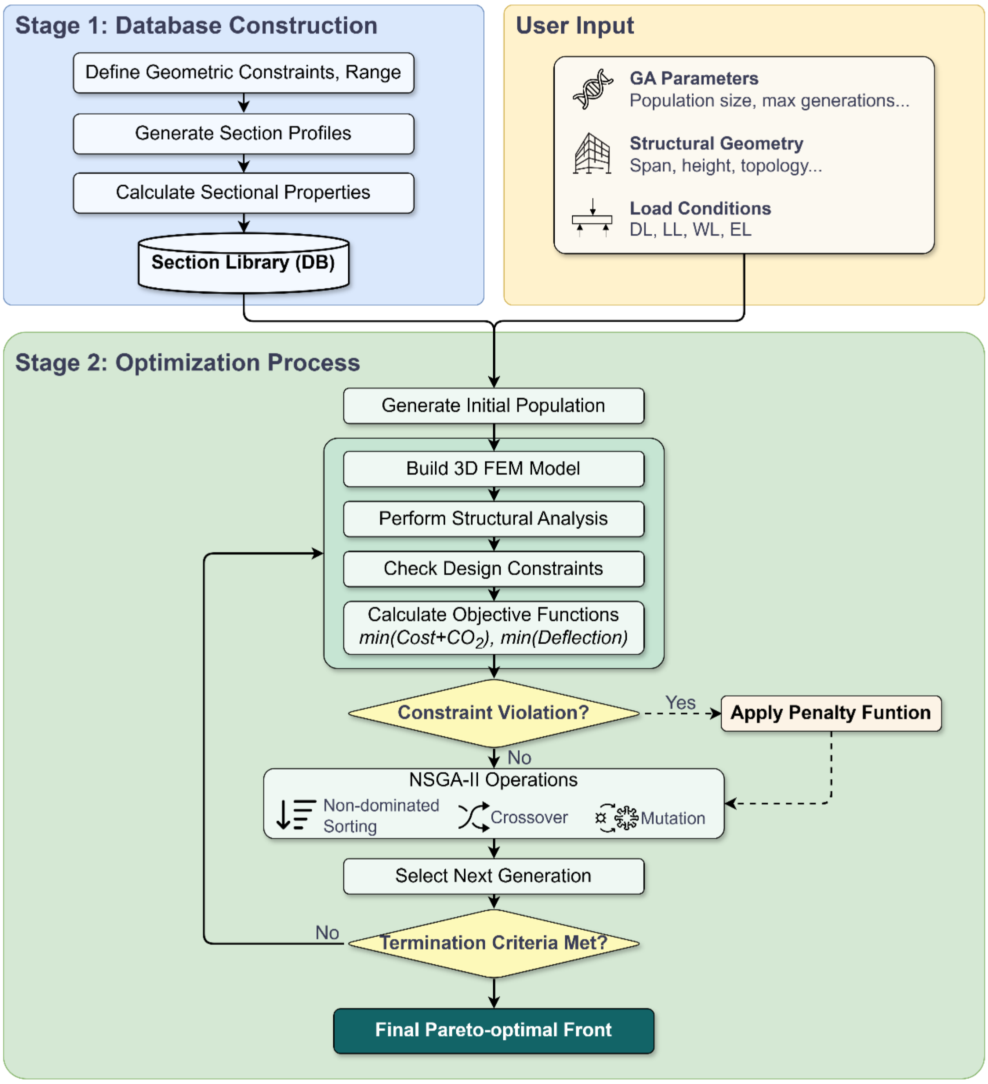

Figure 2. Flowchart of the proposed 3D RC frame optimization framework

3. Optimization methodology

3.1 NSGA-II algorithm and constraint handling

The NSGA-II algorithm employed in this study achieves both convergence and diversity of Pareto optimal solutions through fast non-dominated sorting and crowding distance computation. In particular, to prioritize the search for feasible design solutions in problems where a vast discrete search space coexists with constraints that can only be verified through numerical analysis, the constrained dominance principle is applied. Under this principle, the dominance relation between two individuals X_1 and X_2 is determined based on feasibility status and the total constraint violation ($\Phi(X)$) as follows:

If X_1 is feasible ($\Phi(X_1) = 0$) and X_2 is infeasible ($\Phi(X_2) > 0$), then X_1 dominates.
If both are infeasible, the individual with the smaller violation ($\Phi(X_1) < \Phi(X_2)$) dominates.
If both are feasible, the standard Pareto dominance principle (comparison of objective function values) is applied.

This mechanism guides the algorithm to rapidly converge toward the feasible design region during the early stages of the search, and its effectiveness in large-scale multi-objective optimization problems has been well established [38]. The overall optimization process is illustrated in the flowchart presented in Fig. 2.

3.2 Parametric study of algorithm parameters

To maximize the search efficiency and convergence performance of the NSGA-II algorithm, a five-stage sequential parametric study was conducted in this study using the Hypervolume (HV) indicator as the evaluation criterion. At each stage, the optimal parameter identified in the preceding stage was fixed while the next variable was optimized. The HV is computed in the normalized objective space (f_1, f_2), using a fixed reference point of $(2.0, 2.0)$ that dominates all obtained solutions; because both objectives are normalized to a comparable scale (Eqs. (2) and (5)), this reference point yields a consistent and bounded HV across all examples and runs.

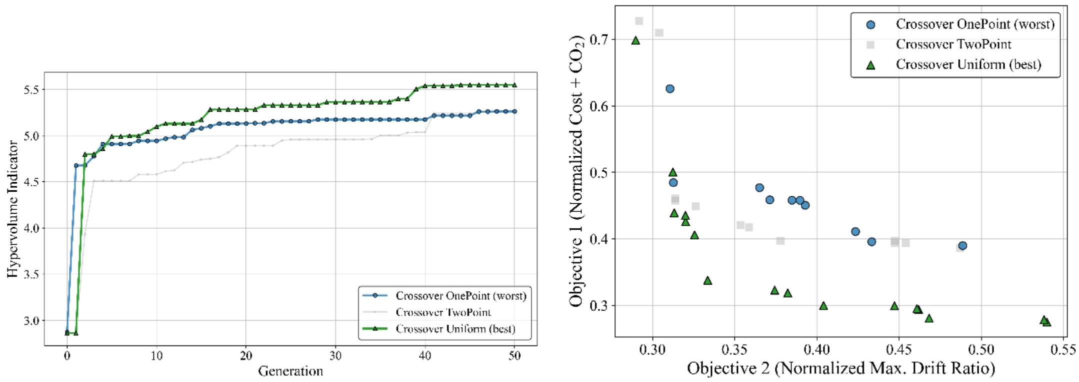

(a) Crossover strategy

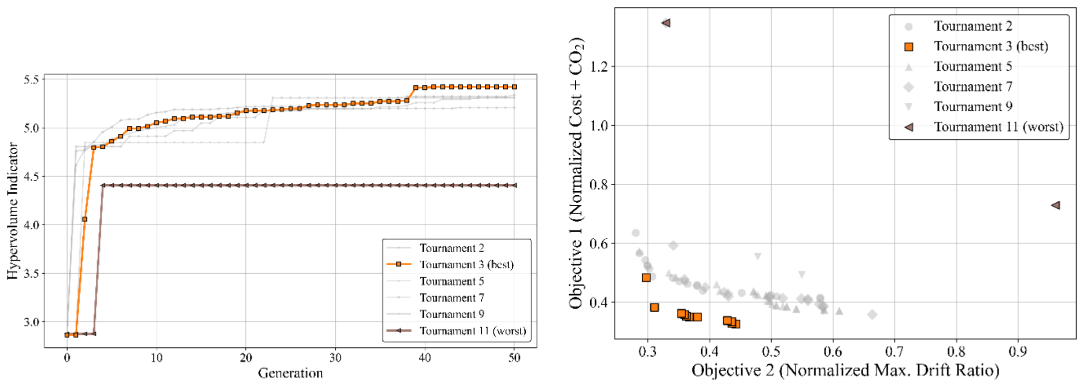

(b) Tournament size

Figure 3. Sequential parameter optimization results

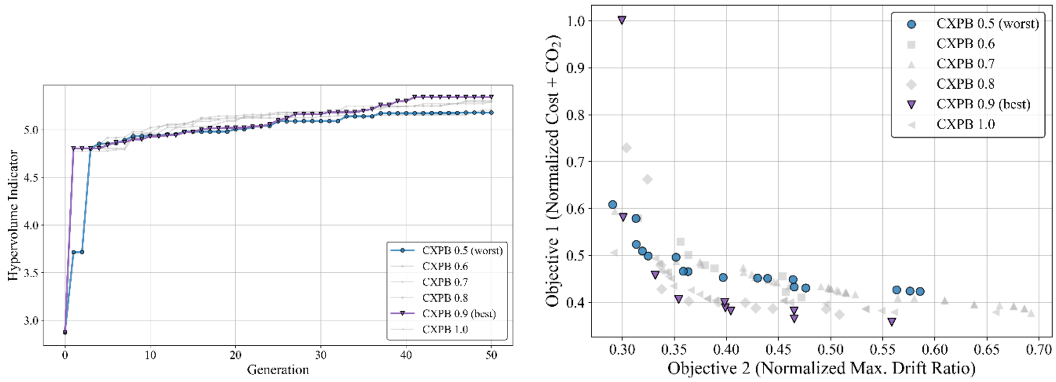

(c) Crossover probability

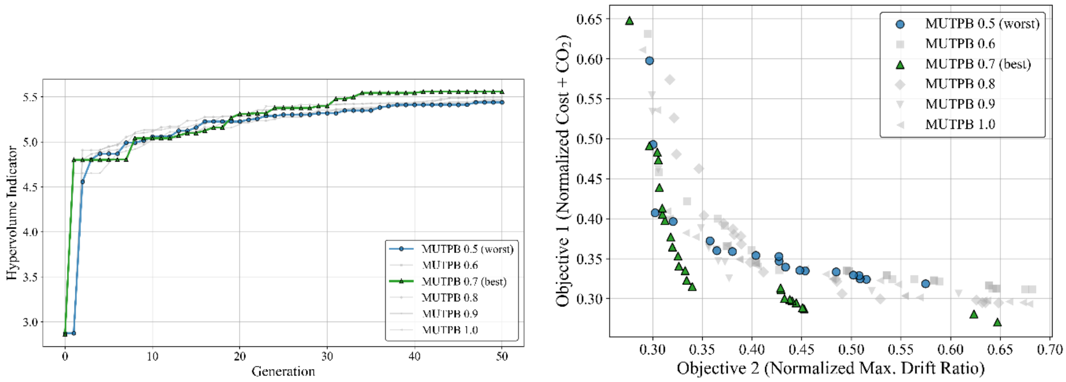

(d) Mutation probability

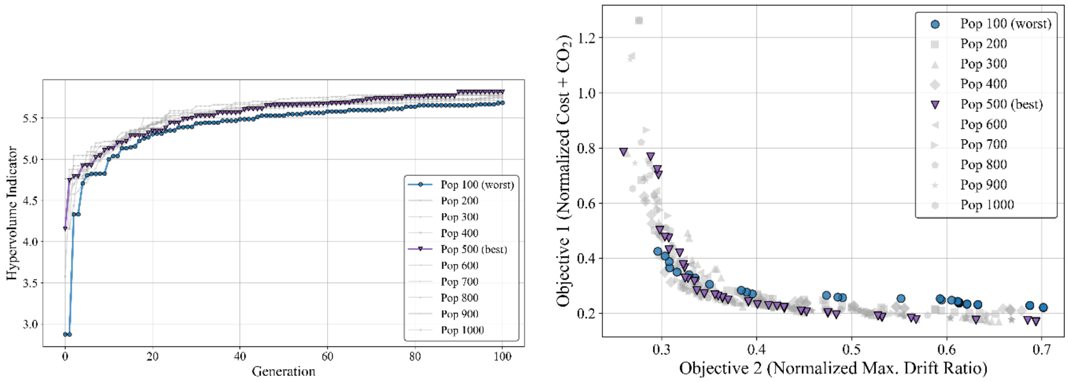

(e) Population size

Figure 3. Continued

To compare convergence performance across crossover strategies, experiments were conducted with One-Point, Two-Point, and Uniform Crossover operators. The results showed that Uniform Crossover exhibited the steepest HV improvement from the early stages of the search and achieved the highest final HV value of approximately 5.55, demonstrating superior performance compared to the other strategies (One-Point: 5.26, Two-Point: 5.27) (Fig. 3(a)).

The tournament size, which controls the selection pressure on parent individuals, was varied from 2 to 11. A tournament size of 3 was found to yield the optimal balance between search diversity and convergence speed. Excessively large tournament sizes induced a bias toward a limited number of elite individuals, causing premature convergence and consequently degrading the diversity of the final solution set (Fig. 3(b)).

To identify the optimal combination of crossover probability (P_c) and mutation probability (P_m), which govern the search intensity of the algorithm, both parameters were varied over the range of 0.5 to 1.0. The experimental results revealed that the combination of a high crossover probability ($P_c = 0.9$) and a relatively high mutation probability ($P_m = 0.7$) yielded the widest Pareto front and the highest HV indicator. In particular, for problems involving discrete section indices as in this study, a high mutation probability was confirmed to play a critical role in escaping local optima and facilitating a global exploration of the design space (Fig. 3 (c), (d)).

Finally, the population size, which determines the global search performance and computational cost of the algorithm, was varied from 100 to 1000. While the HV indicator generally increased with population size, the rate of improvement gradually diminished beyond 500 individuals. Accordingly, considering the trade-off between computational efficiency and solution quality, a population size of 500—the point at which the HV indicator stabilized at approximately 5.817—was adopted as the final optimal value (Fig. 3(e)). It should be noted that this sequential parametric study may not fully capture interaction effects among the parameters; however, the consistent convergence performance observed across ten independent runs in Section 5.3 supports the practical validity of the derived parameter combination.

4. Practical section database and numerical analysis framework

4.1 Project-specific structural section database construction

The optimization framework proposed in this study begins with the construction of a project-specific section database that can flexibly accommodate the required structural performance and practical construction constraints of the target structure. In actual structural design practice, situations frequently arise in which the maximum beam depth is strictly limited due to architectural floor-height restrictions, or only specific grades of concrete and reinforcement are permissible for reasons of constructability and material procurement efficiency. The proposed framework enables the designer to predefine such design scenarios and discretely configure the search space of design variables accordingly. By excluding infeasible section candidates that fail to meet the design requirements, the framework ensures that the optimal design solutions generated by the algorithm can be directly applied to construction practice without further modification. The discrete section ranges applied to the benchmark structures in this paper are summarized in Table 3. The detailing logic for columns and beams is executed through the following process, reflecting practical design guidelines and the provisions of ACI 318-19.

Column detailing (Steps C1-C3): The total longitudinal reinforcement ratio (ρ) of the column section is randomly sampled within the range of 1.0% to 8.0% in accordance with the design code. To satisfy the target reinforcement quantity, the number of longitudinal bars is determined starting from the placement of four corner bars. Depending on the loading characteristics and the cross-sectional geometry, uniaxial reinforcement patterns—in which bars are concentrated along a specific axis—or biaxial reinforcement patterns—in which bars are distributed uniformly on all

Table 3. Discrete section ranges for the 4-story benchmark project database

Parameter	Beam Section	Column Section	Note
Width (b, B)	300 ~ 500 mm	600 ~ 1000 mm	Geometrical constraints
Height (h, H)	500 ~ 800 mm (50 mm step)	600 ~ 1500 mm (50 mm step)	Rectangularity ratio
Concrete (f_{ck})	24, 27, 30 MPa	27, 30, 35, 40 MPa	Member-specific grades
Main Rebar	D16, D22	D25, D29, D32	SD400, SD500
Rebar Ratio (ρ)	ρ_T: $0.3\rho_b$~$0.4\rho_b$ ρ_C: $0.4\rho_T$~$0.5\rho_T$	1.0% ~ 8.0%	ACI 318-19
Stirrup Size	D10, D13	D10, D13	Transverse rebar
Stirrup Spacing	100 ~ 0.5d (max 600 mm)	100 ~ 150 mm	ACI Seismic detailing
Steel (f_y)	400, 500 MPa	400, 500 MPa	Main reinforcement
Aggregate Size	25 mm	25 mm	For spacing/cover

faces—are generated. When the clear spacing between longitudinal bars exceeds the code-specified limit, crossties are automatically placed to ensure adequate lateral confinement. The section capacity is then evaluated by performing $P - M$ interaction analysis in both the strong-axis and weak-axis directions based on strain compatibility.

Beam detailing (Steps B1-B3): To ensure ductility, beam sections are designed as tension-controlled sections by limiting the tension reinforcement ratio (ρ_T) to the range of $0.3\rho_b \sim 0.4\rho_b$ relative to the balanced reinforcement ratio (ρ_b). Additionally, a doubly reinforced beam design is adopted to improve long-term deflection control and constructability. The compression reinforcement ratio (ρ_C) is set at 40% to 50% of the tension reinforcement quantity. When multi-layer bar placement is employed, the variation in clear spacing and the actual effective depth (d) are updated in real time to ensure the accuracy of the nominal flexural strength (M_n) computation. The shear strength is calculated as the sum of the concrete contribution and the stirrup contribution.

For all generated sections, the construction cost and carbon emissions per unit length (1 m) are automatically computed. Carbon emissions are evaluated using a mass-based estimation method that combines the embodied carbon emission factor (ECF) and unit weight of each material, thereby enhancing reliability. The unit weight of each section is also derived for use as input data for the structural analysis model.

In the final stage of the database construction, a Pareto-based smart search space reduction procedure is performed. Within the subset of section candidates sharing the same geometric dimensions and material strength, structurally inefficient sections—those exhibiting inferior structural performance (column: $P - M$ interaction diagram volume; beam: flexural strength) relative to their cost—are eliminated. This process enhances the search efficiency of the optimization algorithm and reduces the computational cost. The complete detailing logic and the Pareto-based reduction procedure are illustrated in Fig. 4.

4.2 Automated structural analysis using OpenSees

The overall optimization framework is implemented by coupling the Python-based DEAP library with the general-purpose structural analysis engine OpenSees [39]. Each design variable

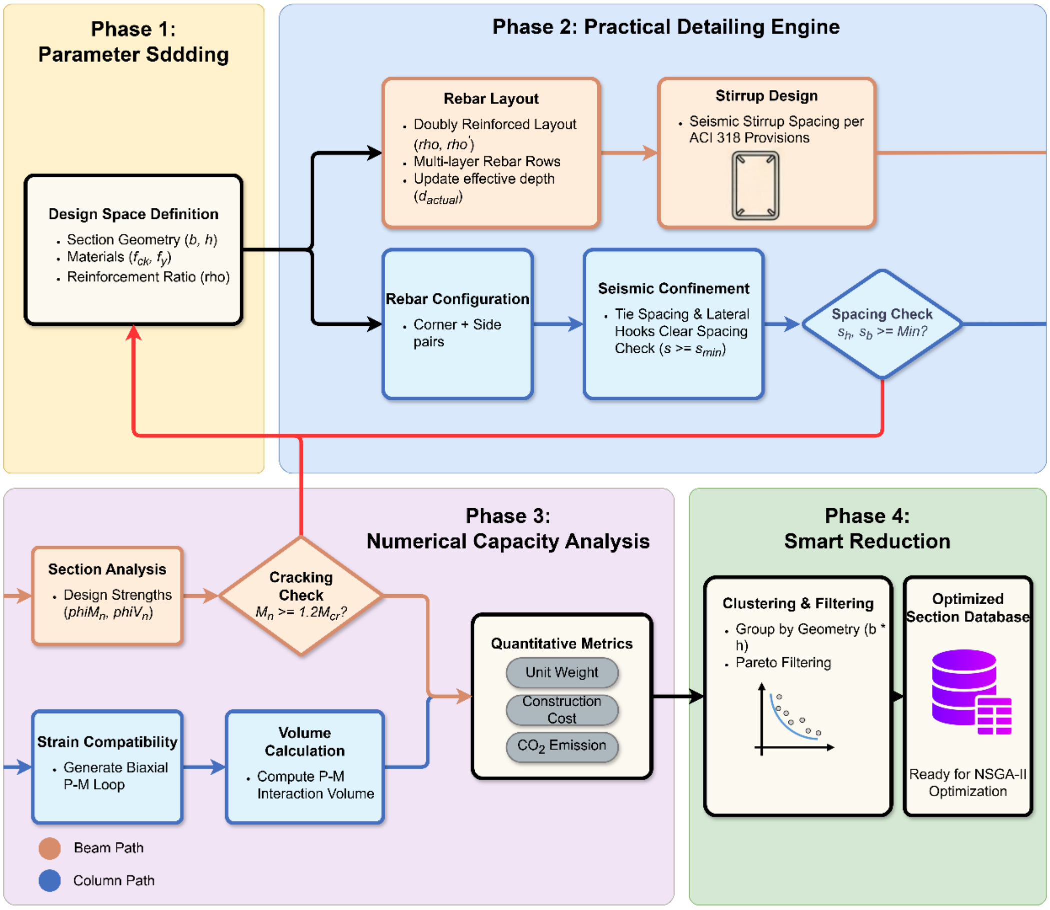

Figure 4. Detailed flowchart of the structural section detailing logic and Pareto-based reduction process

combination generated by the algorithm is automatically converted into a numerical analysis model, and the structural performance of each design alternative is evaluated through OpenSees.

In this study, a refined analysis model incorporating P-Delta effects and the rigid diaphragm assumption was constructed to simulate realistic three-dimensional structural behavior. Load combinations and serviceability checks were performed in accordance with the provisions of ACI 318-19 and ASCE 7-16. Fig. 5 illustrates the geometric configuration, plan irregularity, and three-dimensional loading scenarios of the 4-, 6-, and 8-story benchmark structures employed as examples in this study.

As shown in the figure, the three-dimensional perspective views clearly reveal the plan irregularity of each structure, and in particular, the irregular spans ranging from 5 m to 7 m indicated in the plan views provide a practical design environment in which the directional stiffness imbalance is maximized compared to symmetric configurations. Furthermore, to reflect the assumed building usage and floor-specific characteristics, differential live loads were applied: $5.0\ kN/m^2$ for the lower lobby and neighborhood commercial facility floors (stories 1-2), $3.0\ \mathrm{kN/m^2}$ for the mid-level office spaces (stories 3-5), and $2.0\ \mathrm{kN/m^2}$ for the upper residential and miscellaneous spaces (story 6 and above). The three-dimensional exploded view visualizes

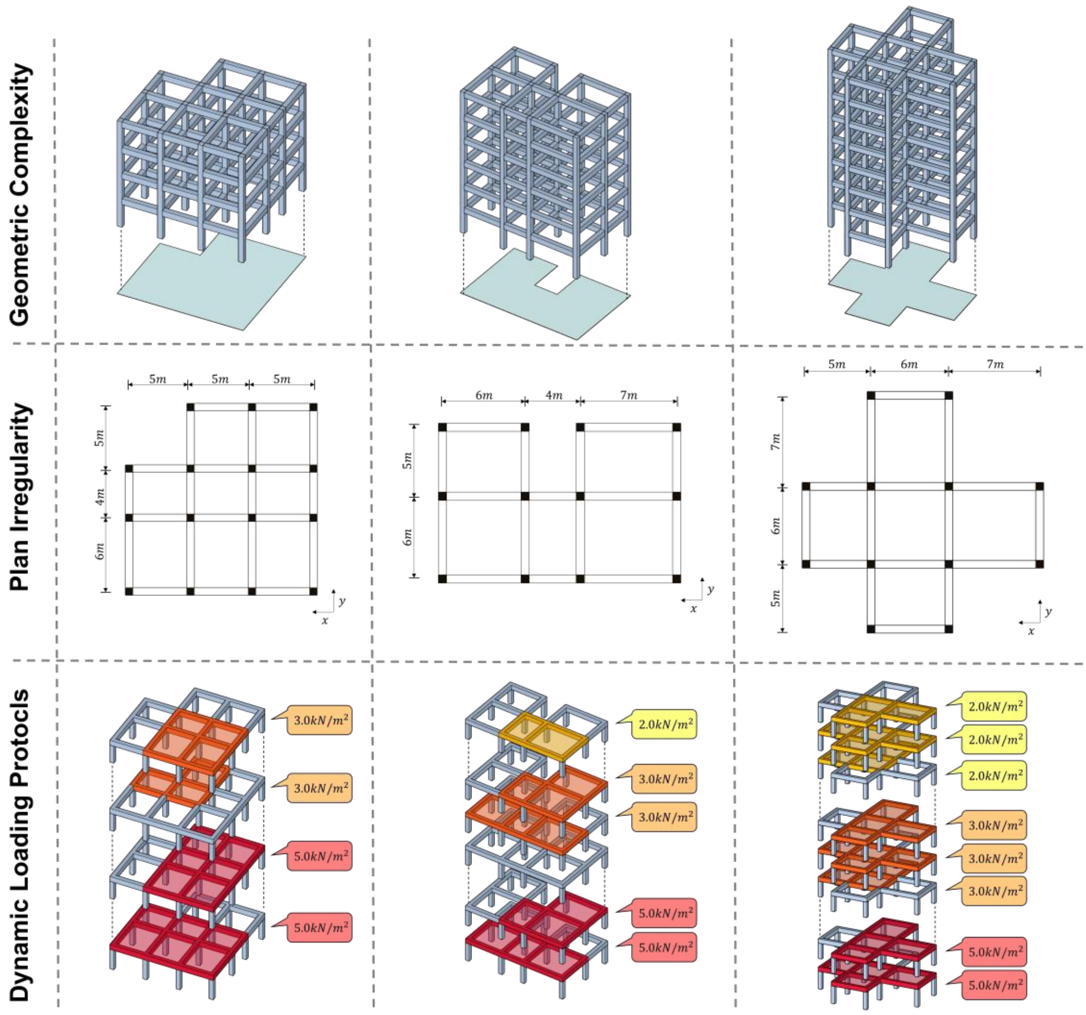

Figure 5. Simulation environment for the benchmark structures: 3D geometry, plan irregularity (irregular spans), and floor-wise checkerboard loading

how these floor-wise load variations and the checkerboard loading pattern alternate vertically across each story. These conditions create distinct local stress states for each member group, posing a challenge that the algorithm must resolve when optimizing column rotation and section sizing.

The checkerboard loading scheme visualized above is essential for simulating the load imbalance arising from differences in building usage and spatial function across floors in practical design. In actual buildings, different live load criteria are applied on a story-by-story or zone-by-zone basis—for lobbies, office spaces, mechanical rooms, and so forth—and such location-dependent load imbalances induce asymmetric stress distributions and eccentricities in specific directions throughout the structure.

In this study, to effectively respond to such practical loading conditions, geometrically efficient rectangular section combinations and a binary rotation variable (R_{dir}) that determines the strong-axis orientation of columns are introduced as design variables in the optimization algorithm. The algorithm actively aligns the strong axis of each column in accordance with the local stress state and the directional stiffness demand of each member group, thereby maximizing the structural resistance capacity within a limited material budget. This approach is differentiated from the conventional design practice that restricts column sections to square shapes or fixes the orientation uniformly, and it serves as a decisive mechanism for forming a customized stiffness distribution optimized for the loading characteristics at each story within the three-dimensional space. The detailed parameters for model construction, the basis for load estimation, and the structural analysis assumptions are described in Appendix A at the end of this paper.

5. Results and discussion

5.1 Analysis of Pareto fronts and representative optimized designs

Application of the proposed optimization framework to the 4-story (Example 1), 6-story (Example 2), and 8-story (Example 3) RC moment frame examples yielded well-defined Pareto fronts in the objective function space for all cases. Fig. 6 presents the distribution of the Pareto fronts in the objective function space for each example.

An analysis of the distribution characteristics of the Pareto solutions with increasing number of stories revealed a pronounced tendency for the structural safety and serviceability constraints to progressively compress the design space as the building height increases. In the 4-story example (Fig. 6(a)), the cost-oriented design solution (Solution ID 1) exhibited a construction cost of approximately 31.74 million KRW with a maximum inter-story drift ratio of 1.786%, whereas the stiffness-oriented design solution (Solution ID 21) raised the construction cost to approximately 93.01 million KRW while reducing the drift ratio to 0.62%, thus offering a wide range of design alternatives.

In contrast, the 6-story example (Fig. 6(b)) and the 8-story example (Fig. 6(c)) exhibited a markedly narrower range of alternatives. In the 8-story case, the minimum-cost design solution (ID 1) corresponded to approximately 63.69 million KRW (1.99% drift), while the maximum-stiffness design solution (ID 23) required approximately 67.95 million KRW (1.29% drift), representing a cost difference of only approximately 6.7%. This indicates that for taller buildings, a minimum level of stiffness must be secured to resist lateral forces, and consequently, a

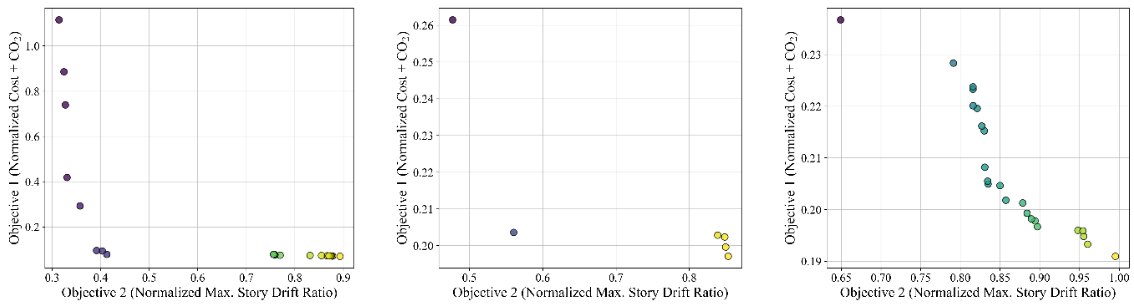

(a) 4-story (b) 6-story (c) 8-story

Figure 6. Multi-objective optimization results in the objective space: Pareto fronts for benchmark structures

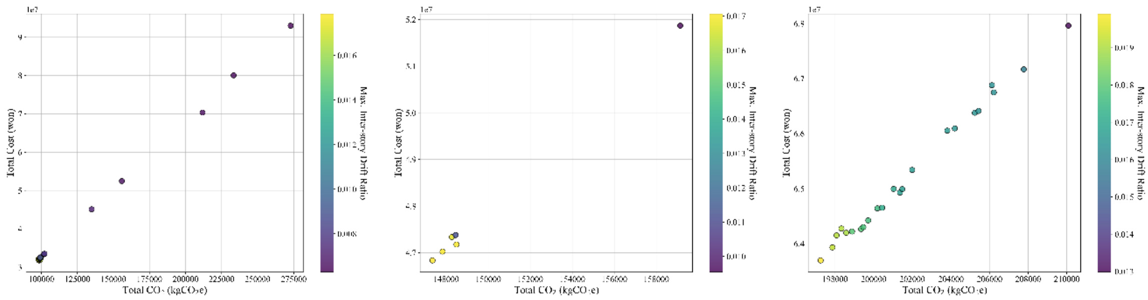

(a) 4-story (b) 6-story (c) 8-story

Figure 7. Distribution of Pareto solutions in the physical space (Total Cost vs. CO_2)

substantial quantity of materials must be invested even during cost-oriented search.

Fig. 7 shows the correlation between the actual construction cost and carbon emissions for each design solution. A very strong positive correlation between the two indicators was maintained across all story-height examples (Pearson correlation coefficient r=0.9998, 0.999 and 0.9959, corresponding to R^2=0.9995, 0.9979, and 0.9917, for the 4-, 6-, and 8-story cases, respectively). In particular, for the 8-story example (Fig. 7(c)), as the construction cost increased from 63.69 million KRW to 67.95 million KRW, the carbon emissions also rose proportionally by approximately 6.5%, from approximately 197,000 kg to 210,000 kg. This proportionality is not coincidental but a direct consequence of the objective formulation: both $Cost(X)$ and $CO_2(X)$ are linear combinations of the identical member-quantity vector (Eqs. (3)-(4)) weighted by fixed unit coefficients, so a near-perfect correlation is structurally guaranteed rather than empirically incidental. The slight departure from $r = 1$ stems solely from the differing cost-to-carbon ratios of concrete, steel, and formwork. Accordingly, Fig. 7 documents this built-in alignment and is not a Pareto front; the genuine trade-off captured by the optimization is the two-dimensional one between the combined economic–environmental objective f_1 and the drift objective f_2. This suggests that, in the multi-objective optimization of three-dimensional RC structures, economic and environmental performance indicators do not conflict with each other and can be managed in an integrated manner. To verify that this alignment is not an artifact of aggregating the two indicators into f_1, a three-objective NSGA-II run treating cost, CO_2, and drift as separate objectives was additionally performed on the 4-story case. The resulting front comprised 61 non-dominated solutions, within which the Cost–CO_2 correlation remained r = 0.9997 (R^2 = 0.9993)—virtually identical to the two-objective value—confirming that the two indicators stay essentially collinear even when optimized independently, and that their aggregation into a single objective entails no loss of trade-off information.

To quantitatively assess the quality of the obtained Pareto fronts beyond the HV indicator, the number of distinct non-dominated solutions, Schott's spacing metric (uniformity; lower is more uniform), and the maximum spread (extent in the normalized objective space) were computed for each example, as summarized in Table 4. (The inverted generational distance (IGD) is not reported, as it requires a known reference Pareto front, which is unavailable for these real-world design problems lacking an analytical optimum; the reference-free metrics above are therefore adopted.) The results confirm the visual observation from Fig. 6: the 4-story case yields a broad and well-populated front (21 solutions, spread 1.20), whereas the 6-story case contains only six distinct non-dominated solutions over a much narrower extent (spread 0.38). This scarcity is not

Table 4. Performance metrics comparison for Solution ID 1 and ID 20 (4-Story)

Example	Non-dominated solutions	Spacing (Δ)	Maximum spread	Pearson r (Cost-CO_2)
4-story	21	0.073	1.195	0.9998
6-story	6	0.070	0.381	0.9990
8-story	23	0.031	0.349	0.9959

Table 5. Performance metrics comparison for Solution ID 1 and ID 20 (4-Story)

Metric	Solution ID 1 (Economical)	Solution ID 20 (High-Stiffness)
Total Cost (KRW)	31,745,592	80,064,699
Embodied CO_2 (kg)	98,504	233,385
Max Story Drift Ratio (%)	1.786%	0.648%
Objective 1 (f_1: Normalized Cost+CO_2)	0.0702	0.8862
Objective 2 (f_2: Normalized Max Drift)	0.8931	0.3241

attributed to premature convergence of the algorithm but to the intrinsic problem structure: the Hypervolume reaches a stable plateau well before the generation limit (Fig. 3) and exhibits very low variance over ten independent runs (Section 5.3), indicating a converged, seed-insensitive search; meanwhile, as the building height increases, the lateral-stiffness requirement progressively dominates the feasible design space, leaving little room for a cost–drift trade-off regardless of search effort. The near-perfect Cost–CO_2 correlation reported above ($R^2 \geq 0.99$) further implies that the first objective behaves as an effectively single dimension; consequently, the genuine trade-off is two-dimensional (combined cost–carbon versus drift), and for the taller frames it contracts toward a near-singular front. The limited diversity of the 6-story case (fewer than ten solutions) is therefore acknowledged as a limitation inherent to stiffness-dominated medium-rise frames rather than an algorithmic deficiency.

To gain deeper insight into the design strategies explored by the optimization algorithm, two representative design solutions (Solution ID 1 and Solution ID 20) located near opposite extremes of the 4-story Pareto front were selected for comparison. The key performance metrics of the two design solutions are compared in Table 5.

Solution 1 adopts an extreme strategy of minimizing the material quantity within the range satisfying all constraints. While minimizing the construction cost and carbon emissions, it permits the maximum inter-story drift ratio to approach the allowable limit (2.0%) at 1.786%, thereby maximizing economic efficiency. In contrast, Solution 20, despite exhibiting an approximately 152% increase in construction cost and a 137% increase in carbon emissions, substantially reduces the maximum inter-story drift ratio to the 0.648% level, thereby dramatically enhancing structural stiffness and serviceability. These two extreme solutions provide the designer with a quantitative basis for selecting the optimal trade-off point according to the project budget and required performance level.

Across all examples, the member demand-capacity ratios (DCR) were maintained at or below 1.0, thereby ensuring structural safety. Notably, as the designs shifted toward the economical end of the Pareto front, the DCR distribution migrated to the 0.7-0.9 range, indicating maximized material efficiency. This demonstrates that the NSGA-II algorithm performed a highly precise search along the constraint boundary. Furthermore, the introduction of the column rotation variable exhibited a particularly pronounced effect on edge columns subjected to eccentric loading.

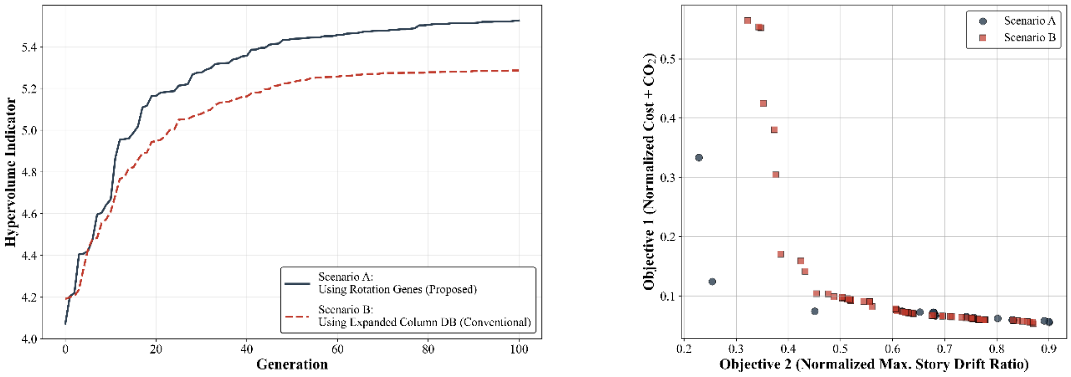

(a) Convergence history of Hypervolume (HV) indicator

(b) Final Pareto front comparison in the objective space (f_1 vs. f_2)

Figure 8. Comparative performance analysis between Scenario A (Proposed: Decoupled) and Scenario B (Conventional: Coupled) under the same random seed

The algorithm automatically aligned the strong axis of the column with the direction of the unidirectional moment transferred from the exterior beams, thereby optimizing the biaxial flexural resistance of the member. The detailed design variable vectors and reinforcement details for each solution are provided in Appendix B.

5.2 Comparative analysis: effect of separate column rotation variables

For clarity, the two compared schemes are defined as follows: Scenario A (proposed) encodes the column section index and its rotation angle as two independent genes, whereas Scenario B (conventional) uses a single gene that selects from a section database pre-expanded to contain both the 0° and 90° orientations. To verify the superiority of the proposed decoupled column rotation variable approach (Scenario A), a comparative analysis was conducted against the conventional approach (Scenario B), in which section selection and rotation are coupled within a single gene, using the 4-story example (Example 1). For experimental rigor, the optimization was performed under identical random seed conditions, and the results are presented in Fig. 8.

The results demonstrated that the proposed Scenario A, which separates the section ID and rotation angle into independent genes, outperformed Scenario B in both search efficiency and final solution quality, despite possessing a longer chromosome structure (32 vs. 20). An analysis of the Hypervolume (HV) indicator (Fig. 8(a)) revealed that Scenario A achieved a final value of 5.5263, representing approximately 4.5% higher convergence compared to Scenario B (5.2865).

This performance advantage stems from the decoupled encoding strategy for the design variables. From the perspective of schema theory in genetic algorithms, Scenario A defines the section specification (attribute) and the rotation angle (directionality) as independent genes, thereby preserving and recombining structurally effective building blocks more effectively without disrupting them. In contrast, Scenario B, which searches through an extensive combined search space of sections and rotations, suffers from the curse of dimensionality, where favorable traits are easily lost through random recombination. Scenario A can rapidly establish the overall stiffness orientation pattern (0/1 pattern) across all members of the three-dimensional frame during the early stages of optimization. Once the optimal strong-axis orientation variables are determined, the algorithm can concentrate its search efficiently within a reduced set of section candidates, rather than exploring a database redundantly inflated with rotation cases as in Scenario B. Consequently, the effective resolution of the search space is enhanced while the search range is simultaneously narrowed, resulting in a dramatic acceleration of convergence speed.

The differences in structural performance are even more pronounced. A comparison of the Pareto fronts in Fig. 8(b) reveals that Scenario A achieved a maximum inter-story drift ratio as low as 0.456% in the high-stiffness design region, whereas Scenario B was limited to the 0.643% level within the same number of evaluations. Moreover, from an economic perspective, the high-performance design solution of Scenario A (ID 26, construction cost of approximately 47.45 million KRW) achieved significantly superior displacement control performance compared to the best stiffness design solution of Scenario B (ID 64, construction cost of approximately 60.97 million KRW), while additionally saving approximately 22% in construction cost. These findings suggest that treating column rotation as a separate variable enables a more precise identification of structurally efficient combinations within the design space.

It should be emphasized that the two scenarios span the identical reachable design space: the conventional database simply pre-expands each column section into its 0° and 90° orientations (doubling the section alphabet from 800 to 1600 entries), whereas the proposed scheme reaches the same set of states through a separate binary rotation gene. The comparison therefore isolates the effect of the encoding strategy alone, and the benefit of the decoupled encoding is most consistent in the early convergence phase, where the orientation pattern can be recombined and mutated independently of the section selection. From a schema-theoretic standpoint, this advantage is expected to become more pronounced as the structural scale increases, since the number of independent orientation variables grows and the decoupled representation can assemble and preserve the orientation building blocks more efficiently than the entangled single-gene representation. The magnitude of this effect at larger scale is, however, problem-dependent rather than predetermined: it is governed by the range and resolution of the section database, the population size relative to the chromosome length, and the degree of plan irregularity and load asymmetry, all of which control how much usable trade-off freedom the feasible space actually retains. Establishing this behavior therefore requires a dedicated parametric study. The present comparison is based on a single matched random seed and is therefore intended as illustrative; a systematic statistical validation over multiple independent seeds and building heights (e.g., a Mann–Whitney U test on Hypervolume and Spacing), with the population size scaled to the problem dimension, entails substantial additional computation and is left as future work.

5.3 Statistical robustness over independent runs

To verify the reliability of the results with respect to the stochastic nature of the genetic algorithm, ten independent optimization runs were performed on the 4-story example (Example 1) under identical conditions with different random seeds. The statistical analysis confirmed that the proposed optimization framework exhibits stable convergence performance.

The mean Hypervolume indicator across the ten runs was 5.2780, and the variation range between the maximum (5.3762) and minimum (5.2421) values was approximately 2.5%, confirming the robustness of the algorithm. This indicates that the framework is not sensitive to initial random seed conditions and can be expected to yield consistent results when used repeatedly in practical design environments. The design solutions derived from all runs formed a clear trade-off relationship between economic efficiency and structural performance, thereby

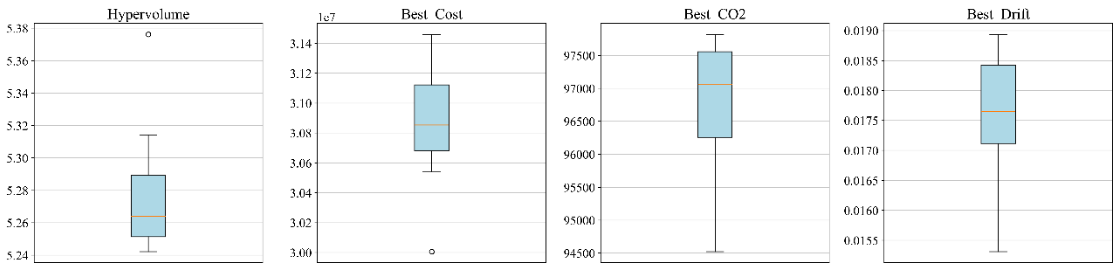

Figure 9. Boxplots of optimization metrics over 10 independent runs: (a) Hypervolume, (b) Best Cost, (c) Best CO2, and (d) Best Drift

supporting the conclusion that the proposed hybrid grouping and gene encoding strategy can be consistently applied to practical building structural design optimization problems. Because the algorithm, constraint-handling scheme, encoding, and parameter settings are identical across building heights, this robustness is expected to carry over to the 6- and 8-story cases; for those stiffness-dominated frames the feasible front is inherently sparse (Table 4), so repeated runs would primarily confirm low variance about a near-singular front. The distribution of the key optimization metrics across the ten runs is visualized in Fig. 9.

6. Conclusions

This study proposed a multi-objective optimization framework for RC moment frames that comprehensively integrates practical reinforcement detailing with three-dimensional structural behavior. Based on the NSGA-II algorithm, Pareto optimal solutions that balance a combined economic–environmental objective (cost and embodied carbon, aggregated into a single dimension) against structural safety, in a two-objective formulation, were derived, and the principal findings are summarized as follows.

Efficiency of decoupled column rotation optimization: The proposed approach (Scenario A), which separates the column section specification and rotation angle into independent genes, demonstrated better performance than the conventional expanded-database approach (Scenario B) in terms of search efficiency. Under an identical random seed, the proposed approach exhibited faster early convergence and an approximately 4.5% higher final Hypervolume in this single-seed comparison, with additional savings of approximately 22% in construction cost and carbon emissions in the high-stiffness design region; since the two encodings span the same design space, this difference is attributable to the encoding strategy. As this comparison is based on a single seed, a multi-seed statistical validation across building heights is identified as future work; the benefit is anticipated to grow with structural scale as the number of orientation variables increases, although the net effect is problem-dependent—contingent on the section-database range, the population size, and the plan irregularity and load conditions—and should be established by that study rather than assumed.

Utilization of a practice-oriented precision database: By establishing a precision detailing logic compliant with ACI 318-19 seismic provisions, along with cost and carbon estimation models, the optimization results achieved a level of reliability that provides a high-fidelity basis for preliminary and elastic-stage design in actual construction practice. This constitutes the core practical value of the present study, distinguishing it from prior research that relies on simplified quantity estimation models.

Variation of design freedom with building height: In the 4-story example, a wide Pareto design range of approximately threefold in cost was observed, whereas in the 8-story example, the cost difference contracted sharply to approximately 6.7%. This indicates that, for taller buildings, the minimum stiffness required for lateral force resistance acts as a physical lower bound on cost optimization, suggesting that differentiated objective function formulation strategies are necessary for the optimization of high-rise structures. Specifically, for frames of six stories and above, the lateral-stiffness requirement dominates the feasible design space, so the Pareto front contracts to a near-singular set (only six distinct non-dominated solutions were obtained for the 6-story case) and the optimization effectively reduces to a single-objective problem. Moreover, the construction cost and embodied carbon were found to be almost perfectly correlated ($R^2 \geq 0.99$ in all examples), indicating that for RC frames designed to ACI 318-19 these two objectives are essentially aligned rather than conflicting; hence their equal-weight summation into a single objective is justified, and the genuine trade-off is between the combined cost–carbon objective and the inter-story drift.

Limitations. The present study has several limitations. The structural evaluation relies on linear-elastic analysis with code-based stiffness reduction ($0.7I_g$ for columns, $0.35I_g$ for beams) and therefore does not capture inelastic redistribution or collapse mechanisms under strong earthquakes; the benchmark set is limited to three irregular frames of low-to-moderate height (4, 6, and 8 stories); and shear-wall or dual lateral-force-resisting systems are not considered. These aspects, together with the near-single-objective behavior observed for taller frames, delimit the scope within which the present conclusions hold.

In conclusion, the optimization framework proposed in this study can serve as a powerful decision-support tool that enables structural engineers to select the optimal trade-off point between economic efficiency and sustainability during the building structural design phase. Future research should extend the framework to composite structural systems incorporating shear walls and advance the optimization methodology by incorporating nonlinear performance-based design (PBD) criteria.

Acknowledgements

This work was supported by the National Research Foundation of Korea (NRF) grant funded by the Korea government (MSIT) (RS-2024-00352968, RS-2026-25471503).

References

1. Ehrgott, M. (2012). Vilfredo Pareto and multi-objective optimization. Documenta Mathematica, 8, 447-453.
2. Esfandiary, M.J., Sheikholarefin, S., Bondarabadi, H.R. (2016). A combination of particle swarm optimization and multi-criterion decision-making for optimum design of reinforced concrete frames. International Journal of Optimization in Civil Engineering, 6(2), 245-268.
3. Marler, R.T., Arora, J.S. (2004). Survey of multi-objective optimization methods for engineering. Structural and Multidisciplinary Optimization, 26(6), 369-395. https://doi.org/10.1007/s00158-003-0368-6.
4. Aga, A.A., Adam, F.M. (2015). Design optimization of reinforced concrete frames. Open Journal of

Civil Engineering, 5(1), 74-83. https://doi.org/10.4236/ojce.2015.51008.
5. Akin, A., Saka, M.P. (2015). Harmony search algorithm based optimum detailed design of reinforced concrete plane frames subject to ACI 318-05 provisions. Computers and Structures, 147, 79-95. https://doi.org/10.1016/j.compstruc.2014.10.003.
6. Aslay, S.E., Dede, T., Kaveh, A. (2024). Integrated design optimization process for building projects. Periodica Polytechnica Civil Engineering, 68(4), 1175-1183. https://doi.org/10.3311/PPci.23377.
7. Babaei, M., Mollayi, M. (2016). Multi-objective optimization of reinforced concrete frames using NSGA-II algorithm. Engineering Structures and Technologies, 8(4), 157-164. https://doi.org/10.3846/2029882X.2016.1250230.
8. Chaudhuri, P., Barman, S., Maity, D., Maiti, D.K. (2021). Cost effective design of RC building frame employing unified particle swarm optimization. Structures, 34, 4356-4374. https://doi.org/10.1016/j.istruc.2021.10.016.
9. Chutani, S., Singh, J. (2018). Use of modified hybrid PSOGSA for optimum design of RC frame. Journal of the Chinese Institute of Engineers, 41(4), 342-352. https://doi.org/10.1080/02533839.2018.1473095.
10. Dehnavipour, H., Mehrabani, M., Fakhriyat, A., Jakubczyk-Galczynska, A. (2019). Optimization-based design of 3D reinforced concrete structures. Journal of Soft Computing in Civil Engineering, 3(3), 95-106. https://doi.org/10.22115/scce.2020.211509.1145.
11. Govindaraj, V., Ramasamy, J.V. (2005). Optimum detailed design of reinforced concrete continuous beams using genetic algorithms. Computers and Structures, 84(1-2), 34-48. https://doi.org/10.1016/j.compstruc.2005.09.001.
12. Kaveh, A., Sabzi, O. (2011). A comparative study of two meta-heuristic algorithms for optimum design of reinforced concrete frames. International Journal of Civil Engineering, 9(3), 193-206.
13. Coello, C.C. (2006). Evolutionary multi-objective optimization: a historical view of the field. IEEE Computational Intelligence Magazine, 1(1), 28-36. https://doi.org/10.1109/MCI.2006.1597059.
14. Deb, K., Pratap, A., Agarwal, S., Meyarivan, T.A.M.T. (2002). A fast and elitist multiobjective genetic algorithm: NSGA-II. IEEE Transactions on Evolutionary Computation, 6(2), 182-197. https://doi.org/10.1109/4235.996017.
15. Nebro, A.J., Galeano-Brajones, J., Luna, F., Coello Coello, C.A. (2022). Is NSGA-II ready for large-scale multi-objective optimization?. Mathematical and Computational Applications, 27(6), 103. https://doi.org/10.3390/mca27060103.
16. Zitzler, E., Thiele, L. (1999). Multiobjective evolutionary algorithms: a comparative case study and the strength Pareto approach. IEEE Transactions on Evolutionary Computation, 3(4), 257-271. https://doi.org/10.1109/4235.797969.
17. Bekdas, G., Nigdeli, S.M. (2014). Optimization of RC frame structures subjected to static loading. Proceedings of the 11th world congress on computational mechanics, Barcelona, Spain, July.
18. Djedoui, N., Djafar-Henni, N., Bekdas, G., Nigdeli, S.M. (2025). Multi-objective optimization of RC structures. Iranian Journal of Science and Technology, Transactions of Civil Engineering, 1-22.
19. Esfandiari, M.J., Urgessa, G.S., Sheikholarefin, S., Manshadi, S.D. (2018). Optimum design of 3D reinforced concrete frames using DMPSO algorithm. Advances in Engineering Software, 115, 149-160. https://doi.org/10.1016/j.advengsoft.2017.09.007.
20. Faghirnejad, S. (2023). Performance-based optimization of 2D reinforced concrete moment frames through pushover analysis and ABC optimization algorithm. arXiv preprint, arXiv:2312.09450.
21. Gharehbaghi, S. (2012). Design optimization of RC frames under earthquake loads. Ph.D. Dissertation, Iran University of Science and Technology, Tehran, Iran.
22. Heydari, F., Andalib, M., Epackachi, S., Rafiee-Dehkharghani, R. (2025). Optimized design of RC moment frames with machine learning methods. Journal of Building Engineering, 104, 112222. https://doi.org/10.1016/j.jobe.2025.112222.
23. Juliani, M.A., Gomes, W.J.D.S. (2021). Optimal configuration of RC frames considering ultimate and serviceability limit state constraints. Revista IBRACON de Estruturas e Materiais, 14(2), e14204. https://doi.org/10.1590/S1983-41952021000200004.

24. Kaveh, A., Ardebili, S.R. (2021). An improved plasma generation optimization algorithm for optimal design of reinforced concrete frames under time-history loading. Structures, 34, 758-770. https://doi.org/10.1016/j.istruc.2021.08.025.
25. Kaveh, A., Ardebili, S.R. (2023a). Optimal design of mixed structures under time-history loading using metaheuristic algorithm. Periodica Polytechnica Civil Engineering, 67(1), 57-64. https://doi.org/10.3311/PPci.20554.
26. Kaveh, A., Ardebili, S.R. (2023b). Optimum design of 3D reinforced concrete frames using IPGO algorithm. Structures, 48, 1848-1855. https://doi.org/10.1016/j.istruc.2023.01.065.
27. Mergos, P.E. (2021). Optimum design of 3D reinforced concrete building frames with the flower pollination algorithm. Journal of Building Engineering, 44, 102935. https://doi.org/10.1016/j.jobe.2021.102935.
28. Mergos, P.E. (2022). Surrogate-based optimum design of 3D reinforced concrete building frames to Eurocodes. Developments in the Built Environment, 11, 100079. https://doi.org/10.1016/j.dibe.2022.100079.
29. Bai, J.L., Chen, H.M., Sun, B.H., Jin, S.S. (2020). Seismic uniform damage-targeted design of RC frame structures. Engineering Mechanics, 37(8), 179-188. https://doi.org/10.6052/j.issn.1000-4750.2019.10.0572.
30. Boscardin, J.T., Yepes, V., Kripka, M. (2019). Optimization of reinforced concrete building frames with automated grouping of columns. Automation in Construction, 104, 331-340. https://doi.org/10.1016/j.autcon.2019.04.024.
31. Kaveh, A., Izadifard, R.A., Mottaghi, L. (2020a). Cost optimization of RC frames using automated member grouping. International Journal of Optimization in Civil Engineering, 10(1), 91-100.
32. Kaveh, A., Izadifard, R.A., Mottaghi, L. (2020b). Optimal design of planar RC frames considering CO2 emissions using ECBO, EVPS and PSO metaheuristic algorithms. Journal of Building Engineering, 28, 101014. https://doi.org/10.1016/j.jobe.2019.101014.
33. Mergos, P.E. (2024). Structural design of reinforced concrete frames for minimum amount of concrete or embodied carbon. Energy and Buildings, 318, 114505. https://doi.org/10.1016/j.enbuild.2024.114505.
34. Oluwole Akadiri, P., Olaniran Fadiya, O. (2013). Empirical analysis of the determinants of environmentally sustainable practices in the UK construction industry. Construction Innovation, 13(4), 352-373. https://doi.org/10.1108/CI-01-2012-0003.
35. Paya-Zaforteza, I., Yepes, V., Hospitaler, A., Gonzalez-Vidosa, F. (2009). CO2-optimization of reinforced concrete frames by simulated annealing. Engineering Structures, 31(7), 1501-1508. https://doi.org/10.1016/j.engstruct.2009.02.034.
36. Werner, W., Burns, J.G. (2012). Quantification and optimization of structural embodied energy and carbon. Proceedings of the structures congress 2012, Chicago, IL, USA, March.
37. ASCE/SEI 7-16 (2016). Minimum design loads and associated criteria for buildings and other structures. American Society of Civil Engineers, Reston, VA, USA.
38. Zavala, G., Nebro, A.J., Luna, F., Coello Coello, C.A. (2016). Structural design using multi-objective metaheuristics. Comparative study and application to a real-world problem. Structural and Multidisciplinary Optimization, 53(3), 545-566. https://doi.org/10.1007/s00158-015-1362-4.
39. Mazzoni, S., McKenna, F., Scott, M.H., Fenves, G.L. (2006). Open system for earthquake engineering simulation (OpenSees) command language manual. Pacific Earthquake Engineering Research Center, University of California, Berkeley, CA, USA.

Appendix A. Structural modeling assumptions and loading parameters

This appendix describes the detailed assumptions of the numerical analysis model and the basis for load estimation referenced in Section 4.2.

Modeling assumptions: The elasticBeamColumn elements employed to simulate the behavior of the three-dimensional frame account for axial force, shear force, torsion, and biaxial bending. P-Delta geometric transformation was applied to the column members to capture higher-order effects, and for rigid diaphragm behavior of the floor slabs, the horizontal degrees of freedom of all nodes at each story were constrained to the corresponding master node. Stiffness reduction follows ACI 318-19 ($0.7I_g$ for columns, $0.35I_g$ for beams), and the specific parameters are summarized in Table A1.

Loading and seismic parameters: Seismic loads are based on the equivalent lateral force procedure of ASCE 7-16, with a response modification coefficient ($R = 5.0$) and a deflection amplification factor ($C_d = 4.5$). Story-level seismic forces are distributed according to the first-mode shape (ϕ) obtained from eigenvalue analysis. Live loads are applied on a differential basis to reflect the floor-wise differences in building usage, ranging from the lobby floors ($\frac{5.0kN}{m^2}$) to the upper residential and office spaces ($2.0 \sim \frac{3.0kN}{m^2}$). For wind load estimation, Exposure Category B for surface roughness was adopted, and the pressure coefficients (C_p) for a basic wind speed of $\frac{30m}{s}$ were taken as 0.8 for the windward face and -0.5 for the leeward face.

Table A1. Detailed structural modeling and loading parameters for benchmark frames

Category	Parameter	Value / Description
Modeling	Element type	3D elasticBeamColumn (6-DOF per node)
	Geometric nonlinearity	P-Delta transformation for columns
	Diaphragm action	Rigid diaphragm (Master-Slave) at each floor
	Effective stiffness	$0.7I_g$ (Columns), $0.35I_g$ (Beams) (ACI 318-19)
Gravity Load	Dead load (Slab+Superimposed)	5.0 kN/m^2 (including 150mm slab)
	Live load (Floor 1-2/3-5/6+)	$5.0/3.0/2.0$ kN/m^2
	Load pattern	Checkerboard pattern per floor
Seismic (ELF)	Design spectral acceleration	$S_{DS} = 0.60g$, $S_{D1} = 0.36g$ (Site Class D)
	Response/Displacement factors	$R = 5.0$, $C_d = 4.5$, $I_e = 1.0$
	Force distribution	First mode shape (ϕ) based (Eigenvalue analysis)
	Directional combinations	100% (Principal)+30% (Orthogonal)
Wind (MWFRS)	Basic wind speed (V)	30 m/s (Exposure B, ASCE 7-16)
	Gust/Pressure coefficients	$G = 0.85$, $C_p = 0.8$ (Windward), -0.5 (Leeward)
Analysis	Total load combinations	38 combinations (Strength: 26, Serviceability: 12)

Appendix B. Design variable sequences and detailed section properties (4-Story)

This appendix provides the design variable configurations and key structural details of the sections employed in the two representative design solutions (Solution ID 1 and Solution ID 20) analyzed in Section 5.1 for the 4-story example. Table B1 presents the story-wise and group-wise section ID and column rotation variable sequences for each representative solution, while Tables B2 and B3 present the detailed structural properties of the column and beam sections applied in those design solutions, respectively.

Table B1. Optimized design variable sequences for representative solutions (Solution ID 1 and ID 20)

Category	Floor	Group Position	Solution ID 1	Solution ID 20
Column Section ID	1F	Corner	4	676
		Edge	7	747
		Interior	15	402
	2F	Corner	47	774
		Edge	28	692
		Interior	8	584
	3F	Corner	170	754
		Edge	11	52
		Interior	11	716
	4F	Corner	201	640
		Edge	157	473
		Interior	28	238
Column Rotation (0: 0°, 1: 90°)	1F	Corner	1	1
		Edge	1	0
		Interior	1	1
	2F	Corner	0	1
		Edge	1	0
		Interior	1	1
	3F	Corner	1	0
		Edge	0	0
		Interior	1	0
	4F	Corner	0	0
		Edge	0	1
		Interior	1	0
Beam Section ID	1F	Exterior	71	436
		Interior	27	351
	2F	Exterior	131	384
		Interior	11	472
	3F	Exterior	90	344
		Interior	27	398
	4F	Exterior	60	404
		Interior	6	436

Table B2. Detailed structural properties of optimized column sections

Item	ID 4	ID 7	ID 8	ID 11	ID 15	ID 28	ID 47	ID 52
Type	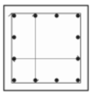	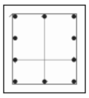	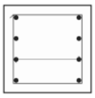	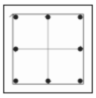	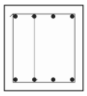	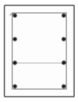	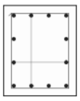	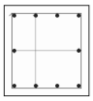
Size	600×600	650×600	600×600	650×650	650×600	800×600	750×600	750×700
Main Bar	12-D25	10-D29	8-D29	8-D32	8-D29	8-D32	12-D29	10-D29
Hoop (Mid)	D10@350	D10@350	D10@150	D13@100	D10@450	D13@350	D10@150	D10@400
Hoop (end)	D10@150	D10@150	D10@100	D13@100	D10@200	D13@150	D10@100	D10@200
Tie Bar	D10	D10	D10	D13	D10	D13	D10	D10

Item	ID 157	ID 170	ID 201	ID 238	ID 402	ID 473	ID 584	ID 640
Type	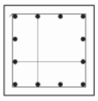	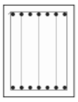	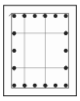	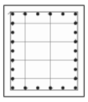	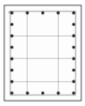	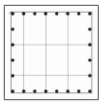	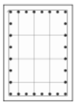	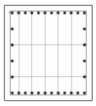
Size	700×700	850×650	900×750	800×700	1050×850	1300×950	1200×850	1100×1100
Main Bar	12-D32	14-D32	16-D25	26-D25	22-D29	28-D29	28-D29	32-D29
Hoop (Mid)	D10@250	D10@200	D10@300	D13@300	D10@200	D13@450	D13@200	D13@200
Hoop (end)	D10@100	D10@100	D10@150	D13@150	D10@100	D13@200	D13@100	D13@100
Tie Bar	D10	D10	D10	D13	D10	D13	D13	D13

Item	ID 676	ID 692	ID 716	ID 747	ID 754	ID 774
Type	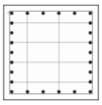	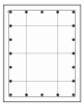	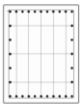	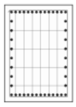	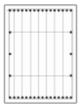	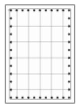
Size	1000×1000	1200×950	1300×1000	1200×850	1300×950	1350×950
Main Bar	26-D32	20-D29	32-D29	44-D29	38-D25	42-D25
Hoop (Mid)	D10@350	D13@350	D13@400	D13@300	D10@400	D13@400
Hoop (end)	D10@150	D13@150	D13@200	D13@150	D10@200	D13@200
Tie Bar	D10	D13	D13	D13	D10	D13

Table B3. Detailed structural properties of optimized beam sections.

Item	ID 6	ID 11	ID 27	ID 60	ID 71	ID 90	ID 131
Type	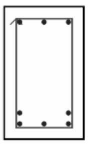	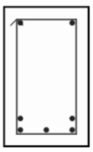	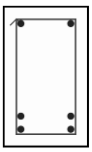	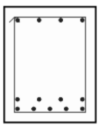	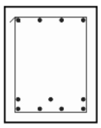	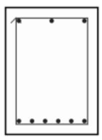	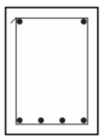
Size	300×500	300×500	300×500	400×500	400×500	400×550	400×550
Main Bar-1 (Top)	3-D16	2-D16	2-D22	4-D16	4-D16	3-D16	2-D22
Main Bar-2 (Bot)	5-D16	5-D16	4-D22	9-D16	7-D16	6-D16	4-D22
Tie Bar (Skin)	-	-	-	-	-	-	-
Hoop (Mid)	D10@100	D10@200	D10@200	D10@200	D10@100	D10@150	D10@100
Hoop (End)	D10@100	D10@100	D10@100	D10@100	D10@100	D10@100	D10@100

Table B3. Continued

Item	ID 344	ID 351	ID 384	ID 398	ID 404	ID 436	ID 472
Type	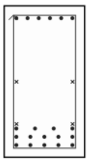	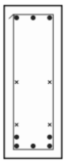	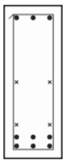	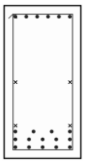		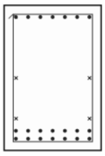	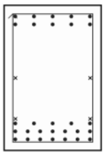
Size	400×750	300×800	300×800	400×800	500×700	500×750	500×750
Main Bar-1 (Top)	5-D16	3-D22	3-D22	5-D16	3-D29	7-D25	10-D25
Main Bar-2 (Bot)	14-D16	5-D22	6-D22	14-D16	7-D29	14-D25	19-D25
Tie Bar (Skin)	4-X	4-X	4-X	4-X	-	4-X	4-X
Hoop (Mid)	D13@100	D13@300	D13@100	D10@250	D13@150	D13@250	D10@100
Hoop (End)	D13@100	D13@150	D13@100	D10@125	D13@150	D13@125	D10@100